

1 Modeling the mechanisms of coastal vegetation dynamics and ecosystem responses to changing  
2 water levels

3 Junyan Ding,<sup>1</sup> Nate McDowell<sup>2,3</sup>, Vanessa Bailey<sup>2</sup>, Nate Conroy,<sup>4</sup> Donnie J. Day,<sup>5</sup> Yilin Fang,<sup>6</sup>  
4 Kenneth M. Kemner,<sup>7</sup> Matthew L. Kirwan,<sup>8</sup> Charlie D. Koven,<sup>9</sup> Matthew Kovach,<sup>5</sup> Patrick  
5 Megonigal,<sup>10</sup> Kendalynn A. Morris,<sup>11</sup> Teri O'Meara,<sup>12</sup> Stephanie C. Pennington,<sup>11</sup> Roberta B.  
6 Peixoto,<sup>5</sup> Peter Thornton,<sup>12</sup> Mike Weintraub,<sup>5</sup> Peter Regier,<sup>13</sup> Leticia Sandoval,<sup>5</sup> Fausto  
7 Machado-Silva,<sup>5</sup> Alice Stearns,<sup>10</sup> Nick Ward,<sup>13</sup> Stephanie J. Wilson<sup>10</sup>

8

- 9 1. Department of Biology, Occidental College, Los Angeles, CA, USA, 90041  
10 2. Biological Science Division, Pacific Northwest National Laboratory, Richland, WA, USA,  
11 99352  
12 3. School of Biological Sciences, Washington State University, PO Box 644236, Pullman, WA,  
13 USA, 99164-4236  
14 4. Earth and Environmental Sciences Division, Los Alamos National Laboratory, New Mexico,  
15 USA, 87545  
16 5. The University of Toledo, Toledo, OH, USA, 43606  
17 6. Earth Systems Science Division, Pacific Northwest National Laboratory, Richland, WA,  
18 USA, 99352  
19 7. Molecular Environmental Sciences Group, Argonne National Laboratory, Lemont, IL, USA  
20 60439  
21 8. Virginia Institute of Marine Science, College of William and Mary, Gloucester Point, VA,  
22 USA, 23062  
23 9. Climate and Ecosystem Sciences Division, Lawrence Berkeley National Laboratory,  
24 Berkeley, USA  
25 10. Smithsonian Environmental Research Center, Edgewater, MD, USA, 21037  
26 11. Joint Global Change Research Institute, Pacific Northwest National Laboratory, College  
27 Park, MD, USA, 20740  
28 12. Environmental Sciences Division, Oak Ridge National Laboratory, Oak Ridge, TN, USA,  
29 37830  
30 13. Marine and Coastal Research Laboratory, Pacific Northwest National Laboratory, Sequim,  
31 WA, USA, 98382

32

33 Corresponding author: Junyan Ding, [jding@oxy.edu](mailto:jding@oxy.edu)

34

35 **Abstract**

36 Coastal forests are increasingly experiencing mortality due to inundation by fresh- and  
37 seawater, leading to their replacement by marshes. These shifts alter vegetation composition,  
38 biogeochemical cycling, carbon storage, and hydrology. Using a hydraulically enabled  
39 ecosystem demography model (FATES-Hydro), we conducted numerical experiments to  
40 investigate the mechanisms behind inundation-driven forest loss and the ecosystem-scale  
41 consequences of forest-to-marsh transitions. We compared mortality processes and their effects  
42 across broadleaf and conifer trees at two coastal sites—Lake Erie (freshwater) and Chesapeake  
43 Bay (saline).

44 Our simulations show that hydraulic failure, driven by root loss under prolonged flooding,  
45 is the primary mortality mechanism across both tree types and sites. Forest replacement by marsh  
46 reduced ecosystem-scale leaf area index (LAI), gross primary production (GPP), transpiration,  
47 and deep soil water uptake in conifer forests, while broadleaf forests experienced smaller  
48 changes due to lower initial LAI and greater marsh compensation. Marsh invasion occurred  
49 following canopy thinning driven by tree mortality. These findings suggest that, under similar  
50 root loss, hydraulic failure dominates coastal tree mortality regardless of species or water type,  
51 with denser forests experiencing stronger ecosystem impacts. Our study identifies key mortality  
52 mechanisms and offers testable hypotheses for future empirical studies on coastal vegetation  
53 change.

54

55

56 **1 Introduction:**

57 Shoreline vegetation provides important ecosystem functions (Barbier et al., 2011; Mitsch et  
58 al., 2015). Coastal forests can be more productive than adjacent upland systems (Tagestad et al.,  
59 2021), have larger carbon stocks than the marshes replacing them (Smith et al. 2021), mitigate  
60 storm-driven erosion (Arkema et al., 2013; Spalding et al., 2014), and provide habitat for a wide  
61 variety of animals (Duarte et al., 2013; Barbier, 2013; Mitsch et al., 2015). Coastal ecosystems  
62 are experiencing rapid increases in tree mortality due to changing water levels in both fresh- and  
63 seawater systems (McDowell et al. 2022). Globally, sea-level rise and flooding threaten coastal  
64 forests, with potential habitat losses ranging from less than 10% with a 1-meter rise to as much  
65 as 55% under a 3-meter rise scenario (Ury et al., 2021). Increasingly variable freshwater levels in  
66 lakes and accelerating sea level rise (SLR) are anticipated with climate change (Varekamp et al.,  
67 1992; Mimura, 2013; Theuerkauf et al., 2019; Kayastha et al., 2022; Saber et al., 2023). Varying  
68 water levels induce large changes in species composition, including shifts from forest to marsh,  
69 driven in part by tree mortality (Keddy and Reznicek, 1986; Hudon, 1997; Frieswyk and Zedler,  
70 2007; Wilcox, 2004; Wilcox and Nichols, 2008).

71 Soil hypoxia and salinity are key drivers of tree mortality under increasing inundation.  
72 Prolonged increases in hypoxia and soil salinity reduce root hydraulic conductance and promote  
73 root loss (Colmer and Flowers, 2008; Pezeshki, 2001). Elevated soil salinity also reduces soil  
74 water potential (Boursiac et al., 2005), thereby reducing the soil-to-root water potential gradient  
75 that drives water movement into roots. Together, these belowground impacts of rising hypoxia  
76 and salinity reduce whole-plant hydraulic conductivity (López-Berenguer et al., 2006; Nedjimi,  
77 2014), subsequently increasing the likelihood of xylem embolism and mortality from hydraulic  
78 failure (McDowell et al., 2022). These reductions in whole-plant conductivity can promote  
79 carbon starvation through declining stomatal conductance (Orsini et al., 2012; Sperry et al.,  
80 2016) and leaf loss (Munns and Termaat, 1986; Wang et al., 2019; Zhang et al., 2021b).  
81 Increased salt concentrations inhibit potassium accumulation in guard cells, also promoting  
82 stomatal closure (Clough and Simm, 1989; Perri et al., 2019). These photosynthetic constraints  
83 can be exacerbated by foliar ion toxicity that impairs photosynthetic biochemistry (Ball and  
84 Farquhar, 1984; Delatorre-Herrera et al., 2021; Munns, 2005; Suárez and Medina, 2006; Li et al.,  
85 2021; Yadav et al., 2011).

86           Physiological impacts from hypoxia and salinity can also vary with the frequency and  
87 duration of inundation and with interspecific variation in physiological traits. Freshwater systems  
88 experience variable inundation across seasons and years (Fig. 1) and may have opportunity to  
89 recover from inundation, whereas SLR induces a chronic rise in inundation that can reduce  
90 recovery (Taherkhani et al., 2020; Thiéblemont et al. 2023). Interspecific trait differences such as  
91 in xylem vulnerability to cavitation can also influence the degree of mortality (Niknam and  
92 McComb, 2000; Lukac et al., 2000; Sairam et al., 2008; Acosta-Motos et al., 2017; Zhao et al.,  
93 2020; McDowell et al. 2022). Mortality mechanism tests have not addressed inundation  
94 dynamics and interspecific variation.

95           Coastal tree mortality has large impacts on ecosystem function (Kirwan and Gedan, 2011).  
96 Tree mortality reduces forest biomass and leaf area (Chen and Kirwan, 2022), which in turn  
97 provides a light environment favorable for the expansion of marsh vegetation (Shaw et al., 2022;  
98 Sward et al., 2023). This results in transpiration and carbon uptake and storage shifting from  
99 trees to marsh plants as forests retreat, with net reductions in fluxes and storage depending on the  
100 degree of compensation by the invading marsh (Smith et al., 2021; Davidson et al., 2018; Zhou  
101 et al., 2023). However, the effects of tree death and marsh invasion on ecosystem-scale fluxes  
102 and their underlying mechanisms are poorly known (Kirwan et al., 2024).

103           In a recent study, Ding et al. (2023b) incorporated the effects of salinity and hypoxia on root  
104 loss, hydraulic function, and photosynthesis into the process-based ecosystem demographic  
105 model FATES-Hydro to simulate physiological responses of conifer trees to seawater exposure.  
106 They applied the model to three coastal conifer forests in the U.S., finding that both hydraulic  
107 failure and carbon starvation contribute to tree mortality, with the dominant mechanism  
108 depending on the rate and duration of salinization. Rapid exposure favored carbon starvation,  
109 while chronic inundation led primarily to hydraulic failure.

110           Building upon Ding et al. (2023b), which focuses on physiological responses of conifer trees  
111 to seawater exposure, here we extend the investigation to broadleaf deciduous trees, allowing  
112 evaluation of how functional traits such as photosynthetic capacity, morphology, and phenology  
113 influence mortality outcomes under similar belowground stress conditions. Because the two tree  
114 types have very different physiology, morphology and phenology, we specifically examine to  
115 which extent the difference in these traits can affect the response of trees to hypoxia and salinity

116 if root loss are the same. We also incorporate a freshwater coastal system (Lake Erie) alongside a  
117 saline coastal site to compare how hydrologic context shapes vegetation transitions. We further  
118 assess ecosystem-scale consequences of tree mortality, including its impact on vegetation  
119 composition, and ecosystem fluxes. We conducted numerical experiments using Ding et  
120 al.(2023b) FATES-Hydro with a reciprocal design where the two tree types were simulated for  
121 both the freshwater and saline coasts to partition the role of species from their environment. We  
122 expect the broadleaf deciduous trees will be more susceptible to carbon starvation particular at  
123 saline coastal than conifers.

## 124 2. Methods

### 125 2.1 Study areas

126 The first site is located on the south shore of Lake Erie (the LE site) in Ohio, USA (41.48°N,  
127 83.06°W) (Fig. S1). The area has warm and humid summers and cold winters. The LE site is  
128 dominated by the broadleaf species shellbark hickory (*Carya laciniosa*) and swamp white oak  
129 (*Quercus bicolor*). Lake Erie is part of the Great Lakes of North America, a series of  
130 interconnected large freshwater lakes. The water level of Lake Erie is subject to daily, seasonal,  
131 interannual, and decadal variation resulting from the complex interactions between climate,  
132 bathymetry, and the water levels of the upper lakes (Burlakova et al., 2014). Increases in the  
133 water levels in Lake Erie have resulted in extensive coastal tree mortality (Sippo et al., 2018;  
134 Theuerkauf and Braun, 2021).

135 The second site is located on the Chesapeake Bay (CB) in Maryland, USA (38.5°N, 76.3°W;  
136 Smith and Kirwan 2021) (Fig. S1). The CB site is dominated by coniferous loblolly pine (*Pinus*  
137 *taeda*) forests, and the climate is characterized by warm, humid summers and cool winters. The  
138 CB region is a hotspot for sea-level driven coastal forest retreat, driven in part by the extensive  
139 low lying coastal plain topography (Schieder et al., 2018; Chen and Kirwan, 2022). In the 21st  
140 century, relative SLR rates in the CB region (~3 to 6 mm per year) are approximately two to  
141 three times faster than the global average (Sallenger et al., 2012; Ezer and Corlett, 2012).

142 In 2022, two forested study plots were established within the dying shoreline forests and in  
143 the neighboring unflooded uplands at each site. Stand level measurements include tree density,  
144 diameter at breast height (DBH) and water table depth. Tree-specific measurements were taken  
145 from eight live trees in each plot, which included growth, non-structural carbohydrates,

146 continues hourly sap flow, leaf gas exchange, leaf photosynthetic capacity, and hourly leaf water  
147 potential (LWP) including predawn and mid-day LWP of a given day during the growing season.  
148 These eight live trees were bored to obtain tree cores for measurements of ring width growth  
149 along with eight dead trees located at the shoreline. We follow exactly the same measurements  
150 and sample processing as described in Zhang et al. (2021), Wang et al. (2020). Here, we  
151 benchmarked the FATES-Hydro model against empirical data collected at each site.

152

## 153 2.2 Numerical experiments with the FATES-Hydro model

154 We conducted numerical experiments at both the LE and CB sites using a newly developed  
155 version of the ecosystem demography model, FATES-Hydro (Ding et al. 2023b), which  
156 represents the physiological impacts of hypoxia and salinity on plants and consequent changes in  
157 root conductance and mortality. All simulations were run with FATES-Hydro within the E3SM  
158 Land Model (ELM). Here we describe this version of FATES-Hydro, its parameterization and  
159 benchmarking for this study, and the design of the numerical experiments.

### 160 2.2.1 Description of FATES-Hydro

161 The Functionally Assembled Terrestrial Ecosystem Simulator (FATES) is a physiology-based  
162 vegetation demographic model that simulates cohort-scale dynamics for different plant  
163 functional types (PFTs) (Fisher et al., 2018; Koven et al., 2020). FATES-Hydro is a version that  
164 integrates the plant hydraulics and their coupling with photosynthesis (Ding et al., 2023a). In  
165 FATES-Hydro plant transpiration is the product of whole-plant leaf area and the transpiration  
166 rate per unit leaf area ( $J$ ), which itself is the product of stomatal conductance and vapor pressure  
167 difference from leaf intercellular spaces to bulk atmosphere. The hydro-dynamic module  
168 represents a plant's roots, xylem, and foliage as a variably porous media (Sperry, Adler,  
169 Campbell, & Comstock, 1998) with conductance and capacitance changing in response to tissue  
170 water potentials dictated by the pressure-volume (P-V) curve and the pressure-conductance  
171 (vulnerability) curve (Manzoni et al. 2013, Christoffersen et al. 2016). Stomatal conductance is  
172 modified from the Ball-Berry model (Ball et al. 1984, Oleson et al. 2013, Fisher et al. 2015) with  
173 a further constraint of leaf water potential through a water stress index  $\beta_t$ , defined by a function  
174 of the ratio of the leaf water potential to the leaf water potential of half stomatal closure ( $P_{50gs}$ )  
175 (Christoffersen et al. 2016). The soil column is divided into 20 layers. The proportion of roots in

176 each layer is calculated from Zeng's (2001) two parameter power law function. Water flow from  
177 each soil layer within the root zone into the plant root system is calculated as a function of the  
178 hydraulic conductance determined by root biomass and root traits such as specific root length,  
179 and the difference in water potential between the absorbing roots and the rhizosphere, and the  
180 transpiration is the sum of root water uptake from all soil layers. Additional technical details and  
181 parameter sensitivity analysis can be found in the technical notes (FATES Development Team,  
182 2021, <https://fates-users-guide.readthedocs.io/projects/tech-doc/en/latest/index.html>) and  
183 publications (e.g. Koven et al., 2020; Xu et al., 2023, Ding et al., 2023a, 2023b, Robbins et al,  
184 2024 ).

185 The version of FATES-Hydro used in this study also includes representation of the  
186 mechanisms by which soil hypoxia and salinity impact tree physiology and mortality (Ding  
187 2023b). The complete description of these new developments can be found in Ding et al.  
188 (2023b). Below we describe the root loss function because this is the key component in this  
189 study.

190 The root loss function ( $kr_{red}$ ), expressed as the proportion of the root conductance under  
191 normal condition, is composed of hypoxia reduction ( $kr_{red,sat}$ ) and the salinity reduction ( $kr_{red,sal}$ ),  
192 expressed as:

$$193 \quad kr_{red} = kr_{red,sat} \cdot kr_{red,sal} \quad \text{Eq.1}$$

194 Each term varies between near zero to 1, with near zero means no roots and 1 means the  
195 roots grow as normal.

196 The hypoxia reduction ratio is given as:

$$197 \quad kr_{red,sat} = \frac{1}{1+b \cdot e^{ks(x-x_0)}} \quad \text{Eq.2}$$

198 where  $b$  and  $ks$  are the scaling parameters that determine the rate of fine root loss from  
199 saturation;  $x$  (hours) is the total duration of the volumetric soil water content [m<sup>3</sup>/m<sup>3</sup>] exceeds  
200 90% saturation over a defined previous period of  $x_0$ . Biologically, parameter  $b$  and  $ks$  can be used  
201 to represent how well the root system of the trees are adapted to waterlogging condition (Fig S2).

202 The salinity reduction ratio is given by a salinity cumulation term ( $acc\_sal$ ) as:

203  $kr_{red,sal} = exp(-kc * acc_{sal})$  Eq.3a

204  $acc_{sal} = max[0, \sum (Sal_{soil,t} - Sal_{cr})]$  Eq.3b

205 where  $kc$  is a parameter determining the rate of fine root loss due to salinity, and  $acc_{sal}$   
206 represents the cumulative salinity stress, calculated by summing the difference between soil  
207 salinity ( $Sal_{soil,t}$ ) and a critical threshold ( $Sal_{cr}$ ) beyond which salinity starts to negatively affect  
208 root mass, over all timesteps (i) up to the current step n. All terms are in PSU. As this  
209 formulation is dependent on the model's timestep, all simulations were run with a fixed temporal  
210 resolution of 30 minutes.

211

## 212 2.2.2 Parameterization and benchmarking

213 For the pine and the salinity induced root loss rate, the parameters used in Ding et al. (2023)  
214 were used in this study. For the broadleaf trees at Lake Erie, the parameters used in FATES-  
215 Hydro were either from field observations or obtained from the TRY trait database (Kattge et al.,  
216 2011) when field observation were not available (Table S1).  $V_{cmax}$  was estimated from A/Ci  
217 curves and then adjusted within the observed range so that the simulated hourly  $A_{net}$  matched the  
218 fitted line of observed values (Fig. S2).  $P50_{gs}$  was adjusted within the ranges of the temperate  
219 broadleaf trees from the TRY database so that the simulated hourly leaf water potential matches  
220 the fitting curved based on measured hourly LWP (Fig. S2).

221 The allometry parameters that define the relationships between diameter at breast height and  
222 total tree height, sapwood area, total woody biomass, and total leaf biomass were estimated  
223 based on values of the Biomass and Allometry Database (BAAD) (Falster et al., 2015). The  
224 complete list of parameters can be found in the GitHub repository:  
225 [https://github.com/JunyanDing/FATES\\_COMPASS](https://github.com/JunyanDing/FATES_COMPASS).

226 To calibrate the plant hydraulic parameters,  $K_{max}$  and xylem vulnerability curves, we first  
227 adjusted the parameters within the observed range of values for our broadleaf species (Kattge et  
228 al. 2011) from TRY database of the site to be close to measured hourly values and then we  
229 adjusted the phenology parameters so that the decline of simulated sap flow matched the  
230 observed pattern (FigS4 top panel). For saturation induced root loss function, based on previous

231 studies (Islam and Macdonald 2004, Aroca et al. 2012, Karlova et al. 2021) and unpublished  
232 experimental observations (B. Wolf unpublished data), we set  $x_0$  to 120 hours (5 days) for this  
233 study. We then adjusted the root loss parameter  $ks$  so simulated sap flow was close to the mean  
234 of the observed values (FigS4 bottom panel) at the shoreline location with observed water table  
235 depth. The simulated average daily sap flow at upland and shoreline locations matches well with  
236 observations (Fig. 2). While perfect agreement is not expected, we find that the model  
237 reasonably captures the seasonal pattern and interannual variability of sap flow.

238 For the marsh grass, we use the biochemical and physiological parameters from O’Meara et  
239 al. (2021) and the allometry (height and total leaf area to stem width ratio) was estimated based  
240 on GCREW data (<https://serc.si.edu/gcrew/data>). Because marsh plants are annual or bi-annual,  
241 phenology and maximum density (number of individuals per ground area), which control the  
242 variation of total leaf area, play a more important role in marsh ecosystems than plant  
243 physiology. We specifically calibrated these parameters. The phenology parameters are  
244 estimated based on the NDVI values from Yaping et al. (2022) and the 2022 field measurement  
245 of sap flow at the LE upland site. The phenology parameters are same for both marsh plants and  
246 broadleaf trees, meaning marsh plant and broadleaf trees have same leaf on and off times. The  
247 NDVI values at the neighboring wetlands indicate the marsh grass system had an LAI  $\sim 2$  ( $\text{m}^2 \text{m}^{-2}$ )  
248 during the peak growing season. We further constrained the maximum density of the marsh to  
249 a growing season LAI of  $2 \text{ m}^2 \text{m}^{-2}$ . To calibrate the broadleaf trees, we ran the model at LE site  
250 in 2022 initialized by the inventory data, then compared the model output with the field  
251 observations of photosynthesis, leaf water potential (Fig S2), and sap flow (Fig S3). We  
252 confirmed that the simulated growth rates over the 30-year simulation period fell within the  
253 observed range of tree ring widths measured from tree cores (Fig S5). Note, our goal was to  
254 assess if simulated growth rates were within the range of observations to enable hypothesis tests,  
255 not to reproduce observed interannual growth variability at the individual tree level.

### 256 *2.2.3 Setup of numerical experiments*

257 The numerical experiments involved three plant functional types (PFT): broadleaf deciduous  
258 tree, evergreen conifer tree, and herbaceous marsh plants. We will call them broadleaf tree,  
259 conifer tree, and marsh plants hereafter. Each simulation was constructed either as broadleaf  
260 tree-marsh or as conifer tree-marsh combination. We first simulated the LE site using its native

261 vegetation, the broadleaf trees and marsh, and the CB site using its native vegetation, conifer  
262 trees, and marsh. We then swapped the tree types between sites, such that the broadleaf forest  
263 was simulated at CB and the conifer forest at LE. The simulations of virtual forests at each site  
264 allowed investigation of how different forest types may respond to the differing drivers, i.e., with  
265 and without salinity. For both experiments we also examined the ecosystem-scale consequences  
266 of forest loss, namely on total evapotranspiration and photosynthetic carbon fluxes.

267 The simulations were driven by the University of East Anglia Climatic Research Unit  
268 (CRU) Japanese Reanalysis (JRA) meteorological product (CRUJRA) (University of East Anglia  
269 Climatic Research Unit; Harris, 2019) for 1990 through 2019. The simulations were initialized  
270 with inventory data of upland locations for the trees at both sites (Fig. S1). We used the observed  
271 inventory data of *Carya spp.* at LE for both CB and LE initialization and observed inventory data  
272 of *Pinus spp.* at CB for both CB and LE initialization. The simulated marsh colonization was  
273 from external seed supply at the first year, then from both external seed supply and local  
274 reproduction afterward.

275 Daily soil salinity and water table depth at CB and water table depth at LE were used as  
276 external driving factors. We used empirically estimated soil salinity at CB, by regression based  
277 on open water level and salinity (Ding et al. 2023b). To estimate water table depth at LE from  
278 1990 to 2019, we obtained the water level of LE at the station in Cleveland  
279 (<https://tidesandcurrents.noaa.gov/inventory.html?id=9063063>). We fit a linear correlation  
280 between the station water level and the observed water table depth at the LE shoreline location in  
281 2022 (Fig 1a), then used this linear model to estimate the daily water depth from 1990 to 2019  
282 via the station water data (Fig 1a). During the simulation period, two floods occurred at LE  
283 (1997–1999 and 2016–2019); at CB, salinity slightly rose around 2002 and 2009, followed by a  
284 constant increase after 2012 (Fig 1d and 1e).

285 Root loss was driven by soil hypoxia (indexed by the duration of saturated water content) for  
286 LE, and both soil hypoxia and salinity for CB. At LE, the root loss was calculated based on water  
287 table depth. The parameters that govern root loss were calibrated based on measured sap flow,  
288 leaf water potential, and loss of plant hydraulic conductance (S1). At CB, the additive root loss  
289 was estimated from soil salinity because soil salinity is highly coupled with hypoxia at CB, and  
290 we used the parameter values from Ding et al. (2023b). Root loss was simulated similarly for

291 both species to explicitly examine the extent to which differences in phenology, leaf and stem  
292 physiology, and the lack of species-specific information on hypoxia and salinity tolerance may  
293 result in different mortality patterns.

294

### 295 3. Results of numerical experiment

#### 296 3.1 Inundation impacts on tree physiology and mortality

297 Inundation had similar impacts on the broadleaf and conifer trees at both LE and CB. Root  
298 loss increased over time as water levels rose (Fig 3a, b). However, root loss differed between  
299 sites, particularly after 2015, due to the differences in inundation dynamics. At LE, root loss  
300 increased each year as water levels rose, but root growth during periods of low water levels  
301 allowed partial recovery. In contrast, the chronic increase in inundation and soil salinity at CB  
302 after 2015 led to ongoing root loss because there was less seasonal variation in water level (Fig.  
303 1c and d), and hence no opportunity for recovering root biomass. This difference in root loss  
304 between sites resulted in sustained reductions in hydraulic conductance ( $k/k_{\max}$ ) at CB after 2015,  
305 whereas both species at LE exhibited some recovery each year (Fig. 3c, d).

306 Despite these site level differences, both LE and CB experienced severe declines in  $k/k_{\max}$   
307 by the end of the simulation period. Non-structural carbohydrates (NSC) showed only slight  
308 variation over the simulation period, suggesting that loss of hydraulic conductance was the  
309 primary process underlying mortality (Fig. 3e, f). This is consistent with observed %NSC at Lake  
310 Erie site (Table S3). Mortality of both the broadleaf and conifer trees increased after 2015, with  
311 higher mortality at CB than LE (Fig. 3g, h). Increasing root loss was associated with declining  
312  $k/k_{\max}$  (Fig. 4a, b) and increased whole-tree mortality (Fig. 4c, d), with no difference between  
313 species. The declines in  $k/k_{\max}$  were strongly associated with increased mortality (Fig. 4).

#### 314 3.2 Ecosystem consequences of forest loss

##### 315 3.2.1 Broadleaf simulations at Lake Erie and Chesapeake Bay

316 We examined the ecosystem-scale consequences of mortality on leaf area index (LAI), gross  
317 primary production (GPP), transpiration ( $E_t$ ), and root water uptake with the broadleaf  
318 simulations at both the LE and CB shoreline sites. In these simulations, the loss of leaf area  
319 through inundation-driven tree mortality was compensated by marsh invasion, resulting in stable

ecosystem-scale LAI over time (Fig. 5a, 5b). GPP and  $E_t$  showed somewhat similar patterns as LAI for both sites, again due to marsh invasion as trees died (Fig. 5c-f). GPP was slightly higher in the shoreline than the upland sites due to the higher GPP of marsh plants, and  $E_t$  showed slight declines below the upland sites (Fig. 5b and 5c). While LAI, GPP, and  $E_t$  all showed relative stability over time, the loss of trees and the marsh invasion led to large changes in the depths of water uptake at both LE and CB. The change in vegetation dominance associated with tree mortality led to an increase in shallow water uptake and a decline in deep water uptake (Fig. 5g-j).

### 3.2.2 *Conifer simulations at Lake Erie and Chesapeake Bay*

The conifer simulations at the shoreline sites at both LE and CB exhibited different patterns than the broadleaf species. LAI, GPP, and  $E_t$  all declined with tree loss, which was not compensated for due to limited marsh invasion (Fig. 6a-f). There was no change in shallow water uptake with changes in vegetation dominance, but there was a large decline in deep water uptake (Fig. 6g-j). As tree LAI declined with mortality, the increase in shallow water uptake observed for broadleaf species was not observed for the conifer species, whereas both species exhibited declines in deep water uptake (Fig. 6).

## 4. Discussion

### 4.1 Summary of Major Findings

We conducted numerical experiments at two coastal sites to investigate the mechanisms driving inundation-driven tree mortality and the subsequent ecosystem impacts and how they differ across tree species and with different inundation regimes. The simulations indicated that root loss was the dominant step driving mortality via hydraulic failure for both species and at both sites (Fig. 3 and 4). Replacement of broadleaf trees by marsh resulted in increased LAI and GPP but reduced  $E_T$  at both sites (Fig 5a to 5f). Replacement of conifer trees by marsh result in reduced LAI, GPP, and  $E_T$  at both sites (Fig. 6a to 6f). Transition from forests to marsh shifted root water uptake from deep to shallow soil layers (Fig 4g, 4h, 6g, 6h). Our numerical experiments suggest that the same mechanisms caused forest loss at both sites regardless of tree type, whereas the ecosystem effects from the replacement of forest by marsh differed between broadleaf and conifer forests. Future empirical studies should be conducted to verify these findings.

## 350 4.2 Tree Level Effects

351 Root loss can promote tree mortality through hydraulic failure and carbon starvation  
352 (McDowell et al., 2022). Our simulations indicated that hydraulic failure is the dominant process  
353 underlying tree mortality for broadleaf and conifer trees at both sites (Fig. 3 and 4). Root loss  
354 resulted in decreased whole tree hydraulic conductance and subsequently xylem conductivity due  
355 to increased xylem embolism (Fig. 4a and 4b). Overall, this led to an increase in tree mortality  
356 (Fig. 4c and 4d). These effects were consistent between LE and CB, although they exhibited  
357 different temporal patterns due to variation in the inundation regimes. Moreover, similar effects  
358 of root loss on plant hydraulics have been documented in both modeling studies (Li et al., 2022;  
359 Ding et al., 2023b) and field studies (Zaerr, 1983; Pezeshki et al., 1996; Andersen et al., 1984;  
360 Islam and Macdonald, 2004; Aroca et al., 2012; Karlova et al., 2021).

361 Reduced hydraulic conductivity can lower leaf water potential and causes stomatal closure.  
362 This mechanism can result in reduced photosynthesis and negative carbon balance, resulting in  
363 reduced capability to maintain tissues and defend against insects and pathogens (McDowell et  
364 al., 2022). However, simulated non-structural carbohydrates (NSC) values (Fig. 3e and 3f)  
365 suggest that carbon starvation was not a major process of tree mortality at the shoreline locations  
366 of both study sites and for both tree types. We had anticipated that broadleaf trees might  
367 experience greater carbon limitation due to higher leaf area and photosynthetic demand.  
368 However, the simulations demonstrated that hydraulic failure associated with root loss occurred  
369 before significant depletion of NSC, leading to similar mortality trajectories between the two  
370 species. This may be due to the rate of inundation-driven root loss relative to the rate of NSC  
371 decline (Ding et al., 2023b). The LE and CB inundation regimes had periods when inundation  
372 declined and the salinity at CB was relatively low, allowing a low level of ongoing  
373 photosynthesis to replenish their NSC pools. Carbon starvation is a slow process due to the time  
374 required to draw down NSCs, whereas hydraulic failure can occur rapidly (McDowell et al.,  
375 2022).

376 Simulated  $k/k_{\max}$  and mortality of broadleaf and conifer trees changed similarly with root  
377 loss (Fig. 4), despite large differences in their leaf economic traits, wood anatomy, crown  
378 allometry, and phenology. This similarity arose because whole-tree  $k/k_{\max}$  can only be as high as  
379 the lowest  $k/k_{\max}$  of any pathway between the soil and foliage. Whole-tree hydraulic conductance

380 is constrained by the lowest conductance along the soil–plant–atmosphere pathway. In our  
381 simulations, root loss strongly reduced soil-to-root conductance, which therefore set the limit for  
382 whole-tree  $k/k_{\max}$ . Thus, traits and processes downstream from the roots became less important  
383 due to the dominant role of root loss in promoting hydraulic failure when it becomes severe (Fig.  
384 3c, d, g, h). Both species are poorly adapted to high levels of hypoxia or salinity, thus root loss  
385 was the critical failure point in tree survival under inundation. Species with root systems adapted  
386 to inundation, such as mangroves, may experience different consequences of increased flooding  
387 that could lead to a larger role of carbon starvation such as through ion toxicity to photosynthesis  
388 and leaf loss (Munns and Termaat, 1986).

389 This convergence in response does not imply that all species react identically to inundation.  
390 Rather, it reflects that under the modeled conditions, root system failure overwhelms the  
391 contributions of other physiological differences. While these results offer mechanistic insights,  
392 the lack of empirical data on species-specific root adaptations remains a limitation. We note that  
393 our parameterizations were based on representative species (*Carya*, *Quercus*, and *Pinus*), which  
394 we treated as proxies for the two tree types. Outcomes may differ among other species within  
395 these groups, therefore we caution against overgeneralization and recommend interpreting these  
396 results as hypothesis-generating rather than conclusive. Future research on the cross-species  
397 variation of root loss and downstream mortality mechanisms, and explicitly test whether these  
398 findings extend to the broader PFT level, will be useful to advance transferable predictive  
399 capacity of coastal vegetation change under increasing inundation.

400

401

#### 402 4.3 Ecosystem-Level Effects Between the Forest Types and Sites

403 The ecosystem-scale consequences of coastal forest loss result both from the loss of trees  
404 and the invasion of marsh plants. We found differences in the ecosystem consequences  
405 associated with species but not sites. As tree mortality associated with soil inundation and/or  
406 salinity progressed, marsh plants invaded broadleaf systems more rapidly than coniferous  
407 systems, thus resulting in different impacts on GPP and  $E_t$ . Marsh plants invaded when LAI  
408 declined below  $1 \text{ m}^2/\text{m}^2$  in both systems (Fig. 5a, 5b and 6a, 6b). The conifer system had higher  
409 stand density than the broadleaf system resulting in initial LAI values of  $\sim 4 \text{ m}^2/\text{m}^2$  and  $\sim 2 \text{ m}^2/\text{m}^2$ ,

410 respectively, thus a much larger amount of mortality was required in the conifer system for LAI  
411 to decline by  $1 \text{ m}^2/\text{m}^2$ ; in other words, when canopy opened hereby facilitated marsh invasion  
412 and establishment. The mortality rates were similar for both species (Fig. 3); thus, the differences  
413 in marsh invasion were due primarily to initial stand structure rather than to species composition  
414 or mortality rates *per se*. The declining LAI in the CB with increasing mortality is consistent  
415 with remotely sensed estimates of the normalized difference vegetation index (Chen and Kirwan  
416 2022), and the rates of marsh invasion are consistent with other observations (Kirwan and  
417 Gedan, 2019; McKown and Burdick, 2024). This resulted in increasing GPP in the broadleaf  
418 system because marsh plants have higher photosynthetic capacity than trees (Pan et al., 2020)  
419 and because ecosystem LAI was higher after marsh invasion into the broadleaf system (Fig. 5c,  
420 5d and 6c, 6d). In contrast, the slower invasion of marsh plants into the conifer system caused  
421 ecosystem level GPP to decline with tree mortality.

422 Replacing broadleaf forest by marsh increased GPP slightly, while  $E_t$  declined slightly (Fig.  
423 7c and 7d). This is likely due to the higher water-use efficiency of marsh plants than trees.  $E_t$   
424 declined with tree mortality in both systems, but more so in the conifer system (Figs 5e, 5f and  
425 6e, 6f). These changes were associated with increased water uptake from shallow soil layer and  
426 reduced uptake from the deep soil layer due to the shallower roots of the marsh plants (Fig. 8)  
427 (Maitre et al., 1999; Schenk and Jackson, 2002). In contrast, conifer mortality resulted in less  
428 marsh invasion and hence reductions in GPP and  $E_t$  (Fig. 7), and water uptake from both shallow  
429 and deep soil layers was greatly reduced due to the loss in conifer roots that were not  
430 compensated by marsh plants (Fig. 8).

431

#### 432 4.5 Future Research

433 Our numeric experiments revealed critical mechanisms regulating vegetation dynamics and  
434 ecosystem impacts in response to SLR. Our study also revealed key next steps to improve our  
435 understanding and model representation. We found that root loss drives large declines in  $k/k_{\text{max}}$   
436 that result in increasing mortality and marsh invasion. However, we did not directly measure root  
437 distribution, but instead calibrated parameters using observed data on leaf water potential, sap  
438 flow, and the  $k/k_{\text{max}}$ . We then applied these calibrated parameters with the assumption that both  
439 the broadleaf and conifer had similar root responses to hypoxia and salinity. This decision was

440 based on three factors. First, we had no species-specific data on root conductance and mortality  
441 in response to hypoxia and salinity. Second, both species live at the shoreline margins of their  
442 respective regions, and thus, we assume they are similar in their root responses. Third, the  
443 rooting depths at both sites are shallow, thus rooting depth may not vary significantly across  
444 species. By setting the root loss parameters the same for both tree species, we investigated  
445 whether differences in phenology, leaf and stem physiology traits result in different mortality  
446 patterns between the two species and found that these trait differences have negligible impacts.  
447 Given the critical role of root conductance and survival, field studies to explore root structure  
448 and function are important next steps for coastal systems. Ecosystem manipulation experiments  
449 can be particularly powerful to untangle the impact of hypoxia and salinity on root loss and  
450 subsequent impacts on physiology and survival, enabling cause-and-effect tests that enable  
451 improved predictive understanding of tree mortality in coastal systems (e.g., Hoppole et al., 2023).

452 The role of changing stand structure during ghost forest formation may be an important  
453 factor impacting marsh invasion, the physiology of surviving trees, and the recruitment of new  
454 trees. Changes in light availability as mortality increases aided marsh invasion and promoted  
455 higher photosynthesis and recruitment (Fig 5a and 5b, Fig 6a and 6b) (Kirwan and Gedan, 2019).  
456 The reduction of water uptake from deep layers may promote hypoxia, salinity, and changes in  
457 redox potential and nutrient cycling. With forest cover, high deep-water uptake can enhance  
458 infiltration of rainfall into deep soil layers, which can bring oxygen rich surface water and  
459 nutrients to these deep layers. Reduced infiltration could result in lower dissolved oxygen in  
460 deep soil (Foulquier et al., 2010), increased salinity (Kirwan et al. in review), changed redox  
461 potential (Rubol et al., 2012), and decreased nutrient availability (Burgin et al., 2010; Burgin et  
462 al., 2012) all of which should feedback to limit vegetation growth. Therefore, quantifying the  
463 rate of marsh invasion, survival of remaining trees, and recruitment of tree seedlings is necessary  
464 to identify mechanisms associated with changing light availability and belowground processes.

465 In addition, it is important to interpret our results in the context of projected future climate  
466 change and sea-level rise. Chesapeake Bay is expected to continue experiencing sea-level rise of  
467 approximately 3–6 mm yr<sup>-1</sup>, about twice the global average, while the Great Lakes are projected  
468 to undergo increasingly variable water levels under climate change (Kayastha et al., 2022;  
469 Sallenger et al., 2012; Ezer and Corlett, 2012). These projections imply that inundation events

470 will become more frequent and prolonged, thereby intensifying the mechanisms identified in our  
471 study, particularly root loss leading to hydraulic failure. Rising temperatures and elevated CO<sub>2</sub>  
472 may further modify these dynamics by altering tree water demand, photosynthetic rates, and  
473 marsh productivity, though the net effects remain uncertain. Together, these changes suggest  
474 heightened vulnerability of both broadleaf and conifer coastal forests to conversion into marshes,  
475 with ecosystem-scale consequences for carbon cycling and hydrology. These broader climate–  
476 hydrology interactions are examined in more detail in a separate manuscript (Ding et al., *in*  
477 *review* at JGR–Biogeosciences), where we provide more detailed projections.

#### 478 4.6 Summary

479 Our numerical experiments indicated that root loss due to coastal inundation served as the  
480 driving force behind the transition from forest to marsh through hydraulic failure-induced tree  
481 mortality. This mechanism resulted in similar physiological consequences for both broadleaf and  
482 conifer trees. However, the transition from forests to marshes led to different ecosystem impacts  
483 between broadleaf and conifer forests due to their different initial LAI. Future research aimed at  
484 enhancing our understanding and representation of the interplay among physiological,  
485 demographic, and stand structural processes in different forest types is necessary for better  
486 predicting vegetation dynamics and ecosystem consequences under SLR.

#### 487 **Acknowledgments**

488 JD, NM, BBL, KM, NW, JPM, PR, SCP, MW, TM, PT, and VB were supported by the  
489 Department of Energy, Biological and Environmental Research program project Coastal  
490 Observations, Mechanisms, and Predictions Across Scales (COMPASS). Any use of trade,  
491 product or firm names is for descriptive purposes only and does not imply endorsement by the  
492 U.S. Government. MK acknowledges the support of the U.S. National Science Foundation  
493 (#1654374, #1832221, #2012670).

#### 494 **Author contributions**

495 JD and NM designed the study and drafted the manuscript. JD developed the model and  
496 performed simulations. CDK helped with model development. NM, NW, LS, DD, KM, MK, PR,  
497 PZ, HZ, SP, SW, WW, WI, AS, TM, and PT collected field data and performed data analysis.  
498 All the authors contributed to the manuscript.

499 **Competing interests**

500 None declared

501 **Code availability statements**

502 The data and FATES-Hydro code that support the findings of this study are openly  
503 available in GitHub repository: [https://github.com/JunyanDing/FATES\\_COMPASS](https://github.com/JunyanDing/FATES_COMPASS) or zendo:  
504 <https://doi.org/10.5281/zenodo.15116449>

505

506 **References**

- 507 Aroca, R., Porcel, R., and Ruiz-Lozano, J. M.: Regulation of root water uptake under abiotic  
508 stress conditions, *J. Exp. Bot.*, 63, 43–57, <https://doi.org/10.1093/jxb/err266>, 2012.
- 509 Acosta-Motos, J. R., Ortuño, M. F., Bernal-Vicente, A., Diaz-Vivancos, P., Sanchez-Blanco, M.  
510 J., and Hernandez, J. A.: Plant responses to salt stress: Adaptive mechanisms, *Agronomy*, 7, 18,  
511 2017.
- 512 Arkema, K. K., Guannel, G., Verutes, G., Wood, S. A., Guerry, A., Ruckelshaus, M., Kareiva,  
513 P., Lacayo, M., and Silver, J. M.: Coastal habitats shield people and property from sea-level rise  
514 and storms, *Nat. Clim. Change*, 3, 913–918, , 2013.
- 515 Barbier, E. B.: Valuing ecosystem services for coastal wetland protection and restoration:  
516 Progress and challenges, *Resources*, 2, 213–230, , 2013.
- 517 Barbier, E. B., Hacker, S. D., Kennedy, C., Koch, E. W., Stier, A. C., and Silliman, B. R.: The  
518 value of estuarine and coastal ecosystem services, *Ecol. Monogr.*, 81, 169–193, 2011.
- 519 Ball, M. C., Farquhar, G. D., and Box, P. O.: Photosynthetic and stomatal responses of two  
520 mangrove species, *Aegiceras corniculatum* and *Avicennia marina*, to long-term salinity and  
521 humidity conditions, *Plant Physiol.*, 74, ,  
522 <https://academic.oup.com/plphys/article/74/1/1/6079345>, 1984.
- 523 Burlakova, L. E., Karatayev, A. Y., Pennuto, C., and Mayer, C.: Changes in Lake Erie benthos  
524 over the last 50 years: Historical perspectives, current status, and main drivers, *J. Great Lakes*  
525 *Res.*, 40, 560–573, 2014.
- 526 Clites, A. H., Smith, J. P., Hunter, T. S., and Gronewold, A. D.: Visualizing relationships  
527 between hydrology, climate, and water level fluctuations on Earth’s largest system of lakes, *J.*  
528 *Great Lakes Res.*, 40, 807–811, , 2014.
- 529 Dasgupta, S. and Meisner, C.: Climate change and sea level rise: A review of the scientific  
530 evidence, , , 2009.
- 531 Davidson, I. C., Cott, G. M., Devaney, J. L., and Simkanin, C.: Differential effects of biological  
532 invasions on coastal blue carbon: A global review and meta-analysis, *Glob. Change Biol.*, 24,  
533 5218–5230, 2018.
- 534 Ding, J., Buotte, P., Bales, R., Christoffersen, B., Fisher, R. A., Goulden, M., Knox, R.,  
535 Kueppers, L., Shuman, J., Xu, C., and Koven, C. D.: Understanding the interplay of rooting and  
536 hydraulic strategies on the response of conifer forest stands to multiyear drought in the Southern  
537 Sierra Nevada of California, *Biogeosciences*, 20, 4491–4510, [https://doi.org/10.5194/bg-20-](https://doi.org/10.5194/bg-20-4491-2023)  
538 [4491-2023](https://doi.org/10.5194/bg-20-4491-2023), 2023.
- 539 Ding, J., McDowell, N., Fang, Y., Ward, N., Kirwan, M. L., Regier, P., Megonigal, P., Zhang,  
540 P., Zhang, H., Wang, W., and Li, W.: Modeling the mechanisms of conifer mortality under  
541 seawater exposure, *New Phytol.*, <https://doi.org/10.1111/nph.19076>, 2023.
- 542 Ding, J. , Nate McDowell, Nate Conroy, Donnie J. Day, Yilin Fang, Kenneth M. Kemner,  
543 Matthew L. Kirwan, Matthew Kovach, Patrick Megonigal, Kendalynn A. Morris, Teri O’Meara,  
544 Stephanie C. Pennington, Roberta B. Peixoto, Peter Thornton, Mike Weintraub, Peter Regier,

545 Leticia Sandoval, Fausto Machado-Silva, Alice Stearns, Nicholas D. Ward, Stephanie J. Wilson ,  
546 Vanessa Bailey: Investigating coastal vegetation dynamics and ecosystem impacts under  
547 elevated CO<sub>2</sub> and temperature: a mechanistic modeling approach, *in review*, JGR-Biogeoscience

548 Duarte, C. M., Losada, I. J., Hendriks, I. E., Mazarrasa, I., and Marbà, N.: The role of coastal  
549 plant communities for climate change mitigation and adaptation, *Nat. Clim. Change*, 3, 961–968,  
550 2013.

551 Du, Y., Zhang, Y., and Shi, J.: Relationship between sea surface salinity and ocean circulation  
552 and climate change, *Sci. China Earth Sci.*, 62, 771–782, 2019.

553 Ezer, T. and Corlett, W. B.: Analysis of relative sea-level variations and trends in the  
554 Chesapeake Bay: Is there evidence for acceleration in sea level rise?, in: *Proc. MTS/IEEE*  
555 *Oceans 2012*, Hampton Roads, USA, 14–19 October 2012,  
556 <https://doi.org/10.1109/OCEANS.2012.6404930>

557 Fisher, R. A., Muszala, S., Versteinstein, M., Lawrence, P., Xu, C., McDowell, N. G., Knox, R.  
558 G., Koven, C., Holm, J., Rogers, B. M., and Spessa, A.: Taking off the training wheels: The  
559 properties of a dynamic vegetation model without climate envelopes, *CLM4.5(ED)*, *Geosci.*  
560 *Model Dev.*, 8, 3593–3619, 2015.

561 Fisher, R. A., Koven, C. D., Anderegg, W. R. L., Christoffersen, B. O., Dietze, M. C., Farnior, C.  
562 E., Holm, J. A., Hurtt, G. C., Knox, R. G., Lawrence, P. J., et al.: Vegetation demographics in  
563 Earth System Models: A review of progress and priorities, *Glob. Change Biol.*, 24, 35–54,  
564 <https://doi.org/10.1111/gcb.13910>, 2018.

565 Friedman, A. R., Reverdin, G., Khodri, M., and Gastineau, G.: A new record of Atlantic sea  
566 surface salinity from 1896 to 2013 reveals the signatures of climate variability and long-term  
567 trends, *Geophys. Res. Lett.*, 44, 1866–1876, 2017.

568 Frieswyk, C. B. and Zedler, J. B.: Vegetation change in Great Lakes coastal wetlands: Deviation  
569 from the historical cycle, *J. Great Lakes Res.*, 33, 366–380, 2007.

570 Gedan, K. B., Kirwan, M. L., Wolanski, E., Barbier, E. B., and Silliman, B. R.: The present and  
571 future role of coastal wetland vegetation in protecting shorelines: Answering recent challenges to  
572 the paradigm, *Clim. Change*, 106, 7–29, 2011.

573 Hopple, A. M., Doro, K. O., Bailey, V. L., et al.: Attaining freshwater and estuarine-water soil  
574 saturation in an ecosystem-scale coastal flooding experiment, *Environ. Monit. Assess.*, 195, 425,  
575 <https://doi.org/10.1007/s10661-022-10807-0>, 2023.

576 Hosoda, S., Suga, T., Shikama, N., and Mizuno, K.: Global surface layer salinity change detected  
577 by Argo and its implication for hydrological cycle intensification, *J. Oceanogr.*, 65, 579–586,  
578 2009.

579 Hudon, C.: Impact of water level fluctuations on St. Lawrence River aquatic vegetation, *Can. J.*  
580 *Fish. Aquat. Sci.*, 54, 2853–2865, 1997.

581 Islam, M. A. and Macdonald, S. E.: Ecophysiological adaptations of black spruce (*Picea*  
582 *mariana*) and tamarack (*Larix laricina*) seedlings to flooding, *Trees*, 18, 35–42, 2004.

583 McKown, J. G. and Burdick, D. M.: Salt marsh migration into coastal uplands and application  
584 for conservation in New Hampshire, Great Bay National Estuarine Research Reserve, 45 pp.,  
585 <https://scholars.unh.edu/jel/681/>, 2024.

586 Karlova, R., Boer, D., Hayes, S., and Testerink, C.: Root plasticity under abiotic stress, *Plant*  
587 *Physiol.*, 187, 1057–1070, 2021.

588 Kayastha, M. B., Ye, X., Huang, C., and Xue, P.: Future rise of the Great Lakes water levels  
589 under climate change, *J. Hydrol.*, 612, 128205, 2022.

590 Keddy, P. A. and Reznicek, A. A.: Great Lakes vegetation dynamics: The role of fluctuating  
591 water levels and buried seeds, *J. Great Lakes Res.*, 12, 25–36, 1986.

592 Koven, C. D., Knox, R. G., Fisher, R. A., Chambers, J. Q., Christoffersen, B. O., Davies, S. J.,  
593 Detto, M., Dietze, M. C., Faybishenko, B., Holm, J., Huang, M., Kovenock, M., Kueppers, L.  
594 M., Lemieux, G., Massoud, E., and Xu, C.: Benchmarking and parameter sensitivity of  
595 physiological and vegetation dynamics using the Functionally Assembled Terrestrial Ecosystem  
596 Simulator (FATES) at Barro Colorado Island, Panama, *Biogeosciences*, 17, 3017–3044,  
597 <https://doi.org/10.5194/bg-17-3017-2020>, 2020.

598 Kirwan, M. L. and Gedan, K. B.: Sea-level driven land conversion and the formation of ghost  
599 forests, *Nat. Clim. Change*, 9, 450–457, 2019.

600 Kirwan, M. L. and Megonigal, J. P.: Tidal wetland stability in the face of human impacts and  
601 sea-level rise, *Nature*, 504, 53–60, 2013.

602 Larcher, W.: *Physiological plant ecology: ecophysiology and stress physiology of functional*  
603 *groups*, Springer, Berlin, 2003.

604 Le Maitre, D. C., Scott, D. F., and Colvin, C.: Review of information on interactions between  
605 vegetation and groundwater, 1999.

606 Lindsey, R.: Climate change: Global sea level, *Climate.gov*, [https://www.climate.gov/news-](https://www.climate.gov/news-features/understanding-climate/climate-change-global-sea-level)  
607 [features/understanding-climate/climate-change-global-sea-level](https://www.climate.gov/news-features/understanding-climate/climate-change-global-sea-level), accessed 14 August 2020, 2021.

608 Lukac, M., Pensa, M., and Schiller, G.: Tree species' tolerance to water stress, salinity, and fire,  
609 in: *Forest Management and the Water Cycle: An Ecosystem-Based Approach*, pp. 247–261,  
610 Springer, Dordrecht, 2011.

611 Manzoni, S.: Integrating plant hydraulics and gas exchange along the drought-response trait  
612 spectrum, *Tree Physiol.*, 34, 1031–1034, <https://doi.org/10.1093/treephys/tpu088>, 2014.

613 McDowell, N. G., Ball, M., Bond-Lamberty, B., Kirwan, M. L., Krauss, K. W., Megonigal, J. P.,  
614 Mencuccini, M., Ward, N. D., Weintraub, M. N., and Bailey, V.: Processes and mechanisms of  
615 coastal woody-plant mortality, *Glob. Change Biol.*, 28, 5881–5900,  
616 <https://doi.org/10.1111/gcb.16297>, 2022.

617 Mimura, N.: Sea-level rise caused by climate change and its implications for society, *Proc. Jpn.*  
618 *Acad. Ser. B*, 89, 281–301, 2013.

619 Mitsch, W. J., Bernal, B., and Hernandez, M. E.: Ecosystem services of wetlands, *Int. J.*  
620 *Biodivers. Sci. Ecosyst. Serv. Manag.*, 11, 1–4, 2015.

621 Niknam, S. R. and McComb, J.: Salt tolerance screening of selected Australian woody species –  
622 a review, *For. Ecol. Manage.*, 139, 1–19, 2000.

623 Munns, R. and Termaat, A.: Whole-plant responses to salinity, *Funct. Plant Biol.*, 13, 143–160, ,  
624 1986.

625 O'Meara, T. A., Thornton, P. E., Ricciuto, D. M., Noyce, G. L., Rich, R. L., and Megonigal, J.  
626 P.: Considering coasts: Adapting terrestrial models to characterize coastal wetland ecosystems,  
627 *Ecol. Model.*, 450, 109561, 2021.

628 Oleson, K. W., Lawrence, D. M., Bonan, G. B., Drewniak, B., Huang, M., Koven, C. D., and  
629 Yang, Z.: Technical description of version 4.5 of the Community Land Model (CLM), NCAR  
630 Technical Note, <https://opensky.ucar.edu/islandora/object/technotes:515>, 2013.

631 Pan, Y., Cieraad, E., Armstrong, J., Armstrong, W., Clarkson, B. R., Colmer, T. D., Pedersen,  
632 O., Visser, E. J. W., Voesenek, L. A. C. J., and van Bodegom, P. M.: Global patterns of the leaf  
633 economics spectrum in wetlands, *Nat. Commun.*, 11, 4519, [https://doi.org/10.1038/s41467-020-](https://doi.org/10.1038/s41467-020-18354-3)  
634 18354-3, 2020.

635 Robbins, Z., Chambers, J., Chitra-Tarak, R., Christoffersen, B., Dickman, L. T., Fisher, R.,  
636 Jonko, A., Knox, R., Koven, C., Kueppers, L., and McDowell, N.: Future climate doubles the  
637 risk of hydraulic failure in a wet tropical forest, *New Phytol.*, 244, 2239–2250, 2024.

638 Saber, A., Cheng, V. Y., and Arhonditsis, G. B.: Evidence for increasing influence of  
639 atmospheric teleconnections on water levels in the Great Lakes, *J. Hydrol.*, 616, 128655, 2023.

640 Sallenger, A. H., Doran, K. S., and Howd, P. A.: Hotspot of accelerated sea-level rise on the  
641 Atlantic coast of North America, *Nat. Clim. Change*, 2, 884–888,  
642 <https://doi.org/10.1038/nclimate1597> , 2012

643 Sairam, R. K., Kumutha, D., Ezhilmathi, K., Deshmukh, P. S., and Srivastava, G. C.: Physiology  
644 and biochemistry of waterlogging tolerance in plants, *Biol. Plant.*, 52, 401–412, 2008.

645 Schenk, H. J. and Jackson, R. B.: The global biogeography of roots, *Ecol. Monogr.*, 72, 311–328,  
646 2002.

647 Shin, S., Gronewold, A. D., Fry, L. M., Hong, Y., Cannon, D., and Fujisaki-Manome, A.: Long-  
648 term hydroclimate trends in the Great Lakes basin: Are there hotspots of regional change?, *J.*  
649 *Hydrol. Reg. Stud.*, 59, 102347, <https://doi.org/10.1016/j.ejrh.2025.102347> , 2025

650 Shepard, C. C., Crain, C. M., and Beck, M. W.: The protective role of coastal marshes: A  
651 systematic review and meta-analysis, *PLoS One*, 6, e27374, 2011.

652 Silliman, B. R., He, Q., Angelini, C., Smith, C. S., Kirwan, M. L., Daleo, P., Renzi, J. J., Butler,  
653 J., Osborne, T. Z., Nifong, J. C., and van de Koppel, J.: Field experiments and meta-analysis  
654 reveal wetland vegetation as a crucial element in the coastal protection paradigm, *Curr. Biol.*, 29,  
655 1800–1806, , 2019.

656 Sippo, J., Lovelock, C. E., Santos, I. R., Sanders, C. J., and Maher, D. T.: Mangrove mortality in  
657 a changing climate: An overview, *Estuar. Coast. Shelf Sci.*, 215, 241–249,  
658 <https://doi.org/10.1016/j.ecss.2018.10.011>, 2018.

659 Smith, I. M., Fiorino, G. E., Grabas, G. P., and Wilcox, D. A.: Wetland vegetation response to  
660 record-high Lake Ontario water levels, *J. Great Lakes Res.*, 47, 160–167, 2021.

661 Spalding, M. D., Ruffo, S., Lacambra, C., Meliane, I., Hale, L. Z., Shepard, C. C., and Beck, M.  
662 W.: The role of ecosystems in coastal protection: Adapting to climate change and coastal  
663 hazards, *Ocean Coast. Manag.*, 90, 50–57, 2014.

664 Sperry, J. S., Adler, F. R., Campbell, G. S., and Comstock, J. P.: Limitation of plant water use by  
665 rhizosphere and xylem conductances: Results from a model, *Plant Cell Environ.*, 21, 347–357,  
666 <https://doi.org/10.1046/j.1365-3040.1998.00287.x>, 1998.

667 Taherkhani, M., Vitousek, S., Barnard, P. L., Frazer, N., Anderson, T. R., and Fletcher, C. H.:  
668 Sea-level rise exponentially increases coastal flood frequency, *Sci. Rep.*, 10, 1–17, , 2020.

669 Theuerkauf, E. J., Braun, K. N., Nelson, D. M., Kaplan, M., Vivirito, S., and Williams, J. D.:  
670 Coastal geomorphic response to seasonal water-level rise in the Laurentian Great Lakes: An  
671 example from Illinois Beach State Park, USA, *J. Great Lakes Res.*, 45, 1055–1068, 2019.

672 Thiéblemont, R., Le Cozannet, G., D’anna, M., Idier, D., Belmadani, A., Slangen, A. B., and  
673 Longueville, F.: Chronic flooding events due to sea-level rise in French Guiana, *Sci. Rep.*, 13,  
674 21695, 2023.

675 Theuerkauf, E. J. and Braun, K. N.: Rapid water level rise drives unprecedented coastal habitat  
676 loss along the Great Lakes of North America, *J. Great Lakes Res.*, 47, 945–954, 2021.

677 Ury, E. A., Yang, X., Wright, J. P., and Bernhardt, E. S.: Rapid deforestation of a coastal  
678 landscape driven by sea-level rise and extreme events, *Ecol. Appl.*, 31, e02339, 2021.

679 Varekamp, J. C., Thomas, E., and Van de Plassche, O.: Relative sea-level rise and climate  
680 change over the last 1500 years, *Terra Nova*, 4, 293–304, 1992.

681 Vineis, P., Chan, Q., and Khan, A.: Climate change impacts on water salinity and health, *J.*  
682 *Epidemiol. Glob. Health*, 1, 5–10, 2011.

683 Wilcox, D. A.: Implications of hydrologic variability on the succession of plants in Great Lakes  
684 wetlands, *Aquat. Ecosyst. Health Manag.*, 7, 223–231, 2004.

685 Wilcox, D. A. and Nichols, S. J.: The effects of water-level fluctuations on vegetation in a Lake  
686 Huron wetland, *Wetlands*, 28, 487–501, 2008.

687 Zeng, X.: Global vegetation root distribution for land modeling, *J. Hydrometeorol.*, 2, 525–530,  
688 2001.

689 Zhao, C., Zhang, H., Song, C., Zhu, J. K., and Shabala, S.: Mechanisms of plant responses and  
690 adaptation to soil salinity, *The Innovation*, 1, 100017, 2020.

691 Zhang, P., McDowell, N. G., Zhou, X., Wang, W., Leff, R. T., Pivovarov, A. L., Zhang, H.,  
692 Chow, P. S., Ward, N. D., Indivero, J., and Yabusaki, S. B.: Declining carbohydrate content of  
693 Sitka-spruce trees dying from seawater exposure, *Plant Physiol.*, 185, 1682–1696,  
694 <https://doi.org/10.1093/plphys/kiab002>, 2021.

695 Zhou, J., Zhang, J., Chen, Y., Qin, G., Cui, B., Lu, Z., Wu, J., Huang, X., Thapa, P., Li, H., and  
696 Wang, F.: Blue carbon gain by plant invasion in saltmarsh overcompensated carbon loss by land  
697 reclamation, *Carbon Res.*, 2, 39, 2023.

698

699 **Figure caption**

700 Fig.1 Study area: a) relation between lake depth and soil water table depth in 2022, at the Lake  
701 Erie site transition zone corresponding to the shoreline location in simulations; b) depth of Lake  
702 Erie 1990–2020; c) Estimated water table depth at Lake Erie (LE) shoreline location; d) sea level  
703 and open water salinity of the nearby station of Chesapeake Bay (CPB); and e) Estimated soil  
704 salinity at CPB site

705  
706 Fig.2 Benchmark root loss function by comparing measured and simulated average daily sap  
707 flow of Aug and Sep. 2022 at upland location and shoreline location at LE site

708  
709 Fig.3 Simulated tree level variables of shoreline forest at Lake Erie and Chesapeake Bay: a) and  
710 b) monthly mean % live root; c) and d) monthly mean  $k/k_{max}$ ; e) and f) annual %NSC; g) and h)  
711 annual mortality rate

712  
713 Fig.4 Simulated relation between a) and b) mean growing season  $k/k_{max}$  and % live roots of tree;  
714 c) and d) annual mean mortality and % live roots of tree

715  
716 Fig.5 Ecosystem effects of broadleaf forest at Lake Erie and Chesapeake Bay: a) and b) mean  
717 growing season leaf area index (LAI); c) and d) gross primary productivity (GPP); e) and f)  
718 transpiration ( $E_t$ ); g) and h) root water uptake rate from shallow soil; i) and j) root water uptake  
719 rate from deep soil at shoreline (SH) and upland (UP) locations

720  
721 Fig.6 Ecosystem effects of conifer forest at Lake Erie and Chesapeake Bay: a) and b) mean  
722 growing season leaf area index (LAI); c) and d) gross primary productivity (GPP); e) and f)  
723 transpiration ( $E_t$ ); g) and h) root water uptake rate from shallow soil; i) and j) root water uptake  
724 rate from deep soil at shoreline (SH) and upland (UP) locations

725  
726 Fig.7 Change in gross primary productivity (GPP) (a and b) and transpiration ( $E_t$ ) (c and d) with  
727 tree abundance of shoreline forests as indicated by tree LAI at Lake Erie and Chesapeake Bay

728  
729 Fig.8 Change in water uptake from shallow soil layer (a and b) and from deep soil layer (c and d)  
730 with tree abundance of shoreline forests as indicated by tree LAI at Lake Erie and Chesapeake  
731 Bay

732  
733

# Figures

Fig.1

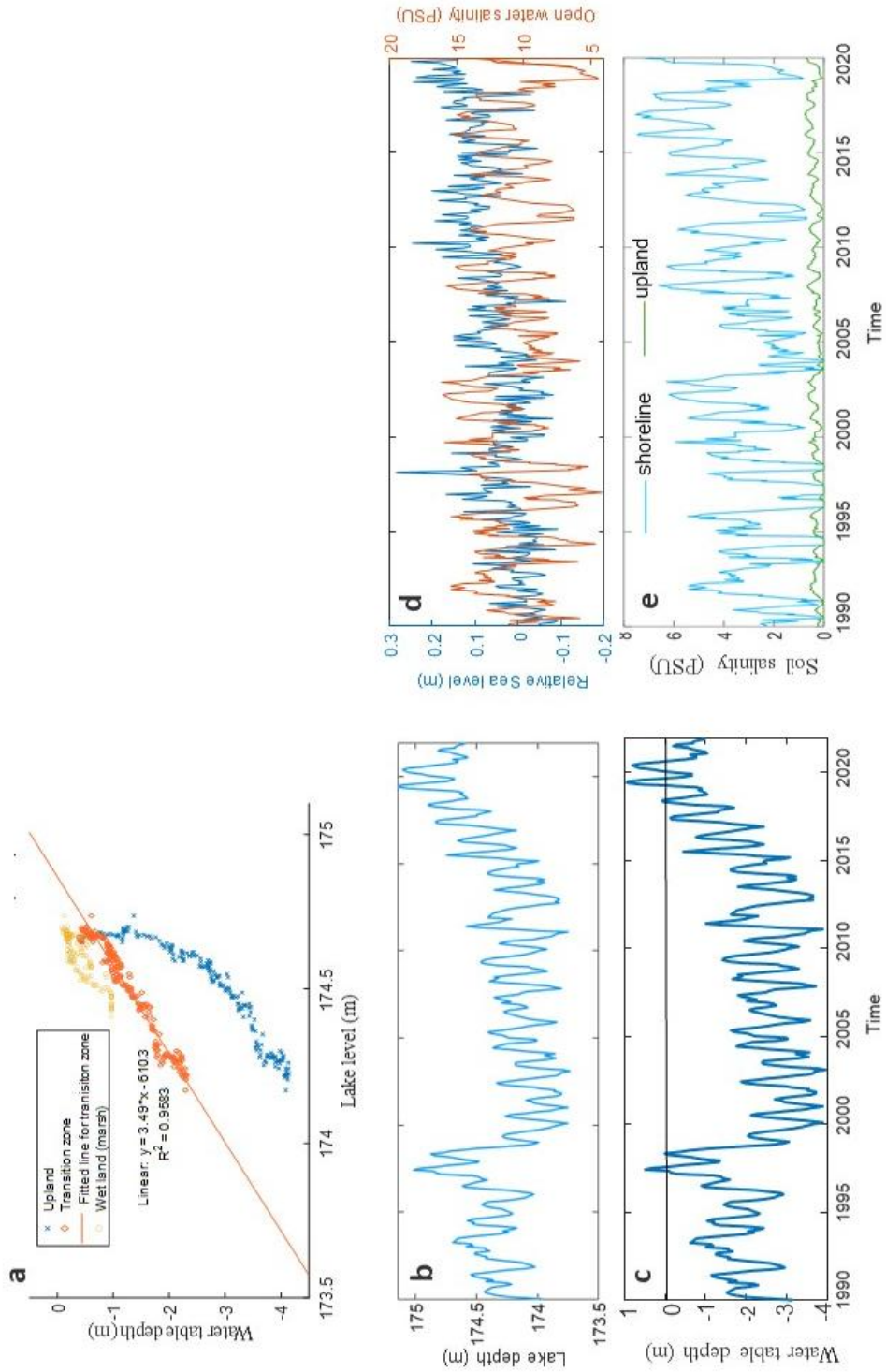


Fig. 2

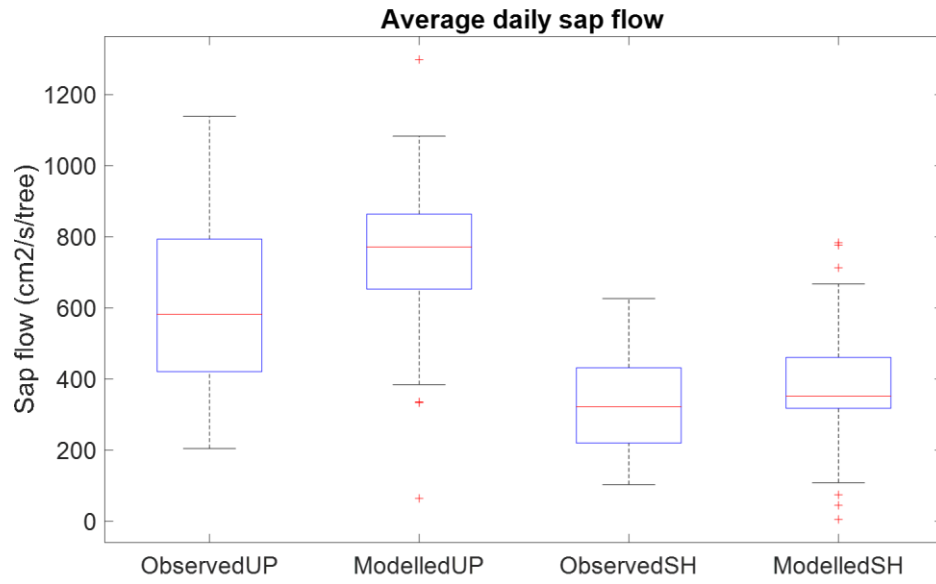


Fig.3

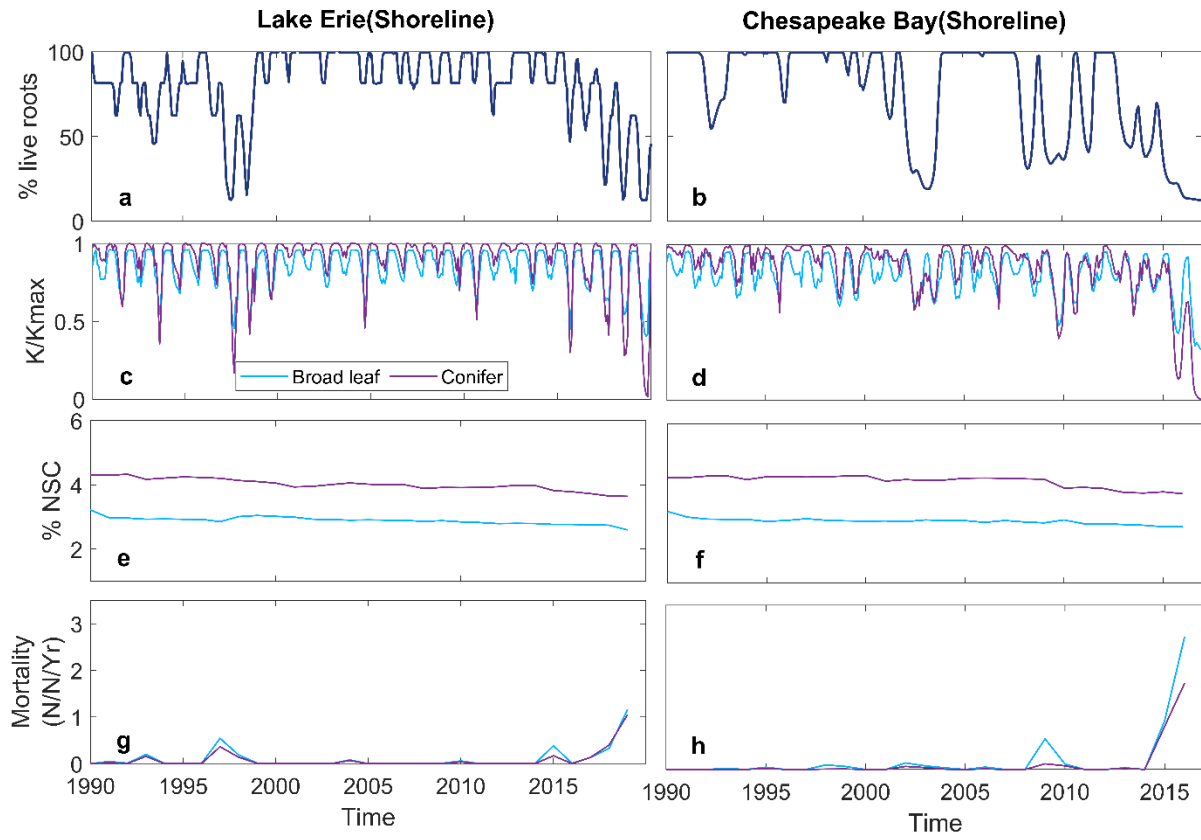


Fig.4

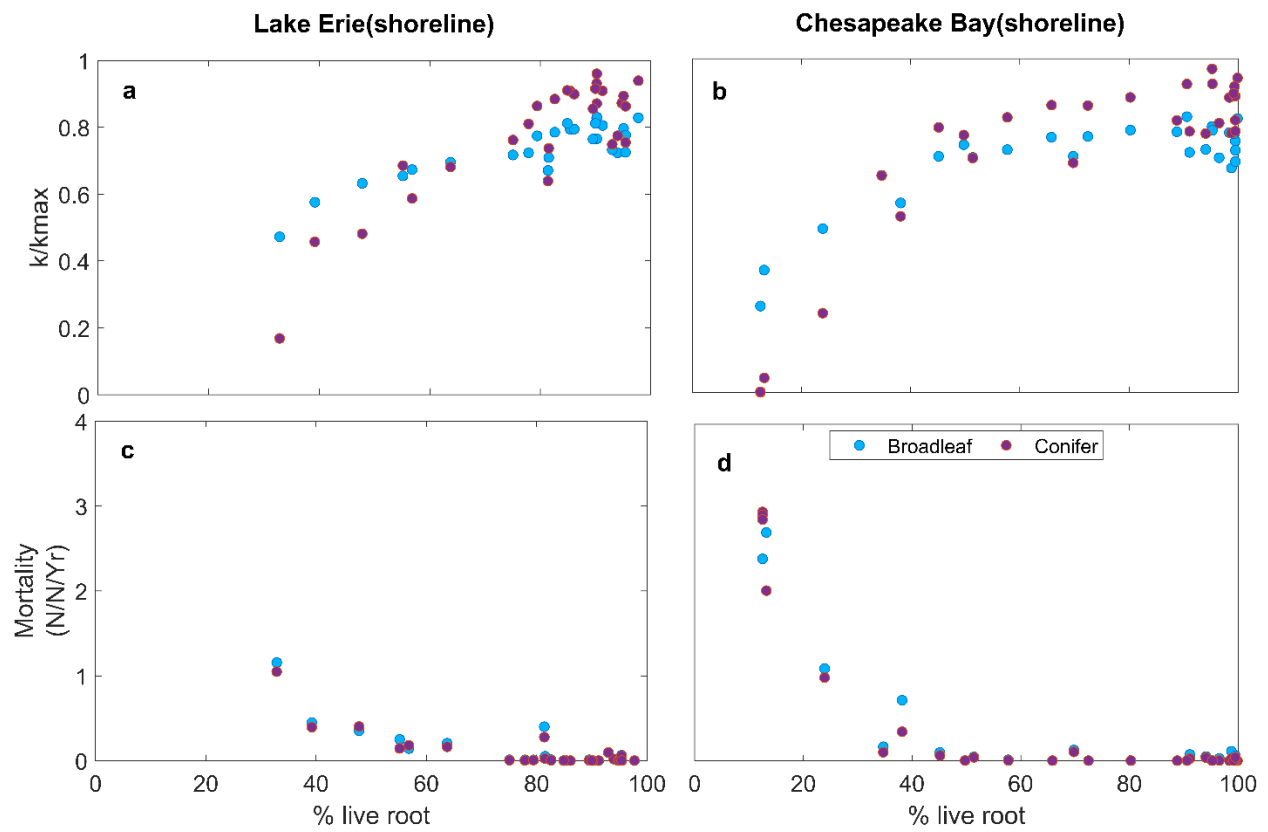


Fig.5

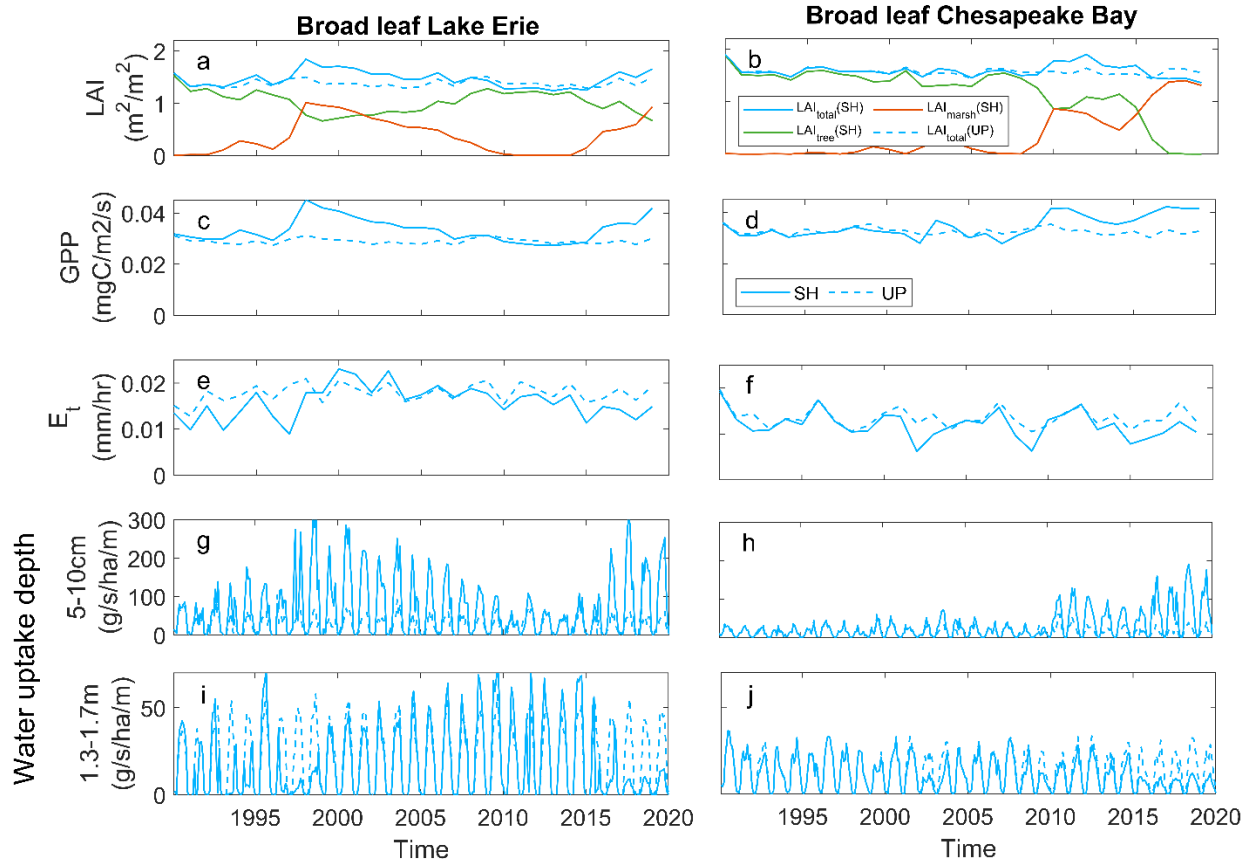


Fig.6

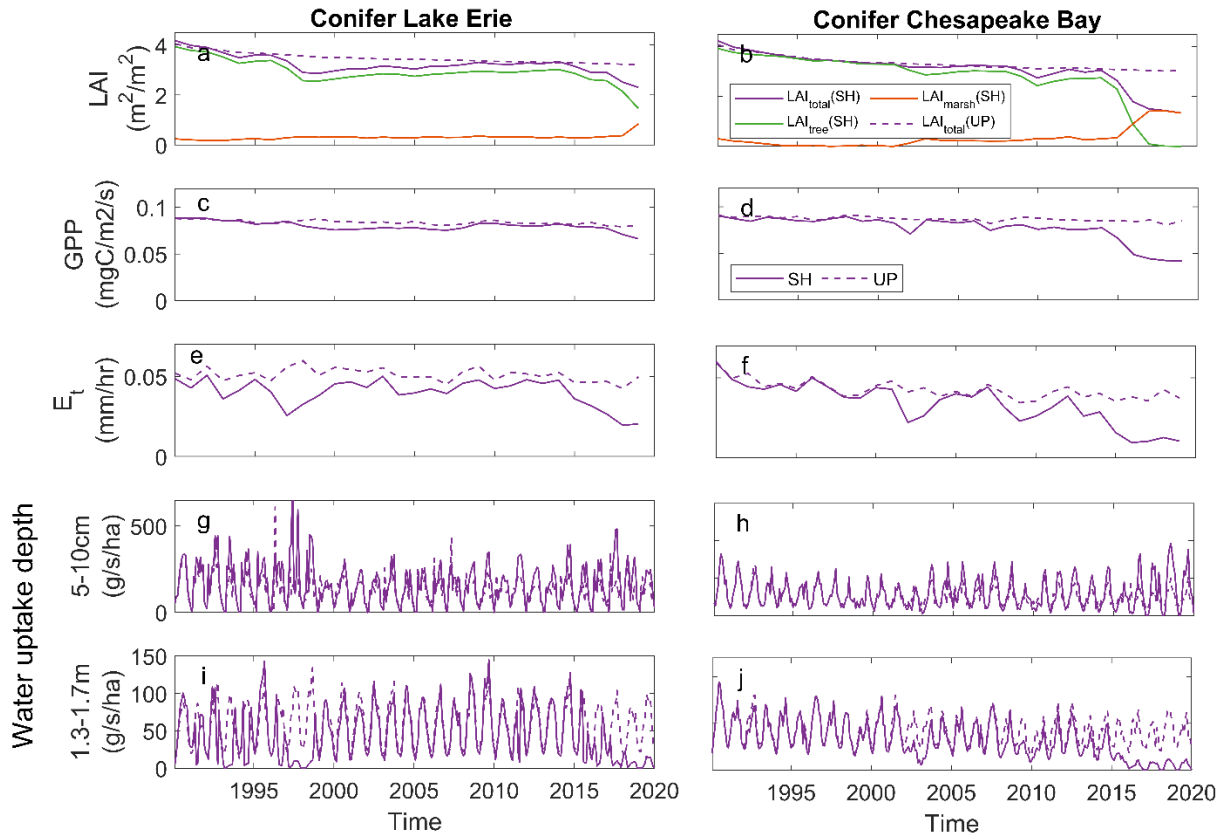


Fig. 7

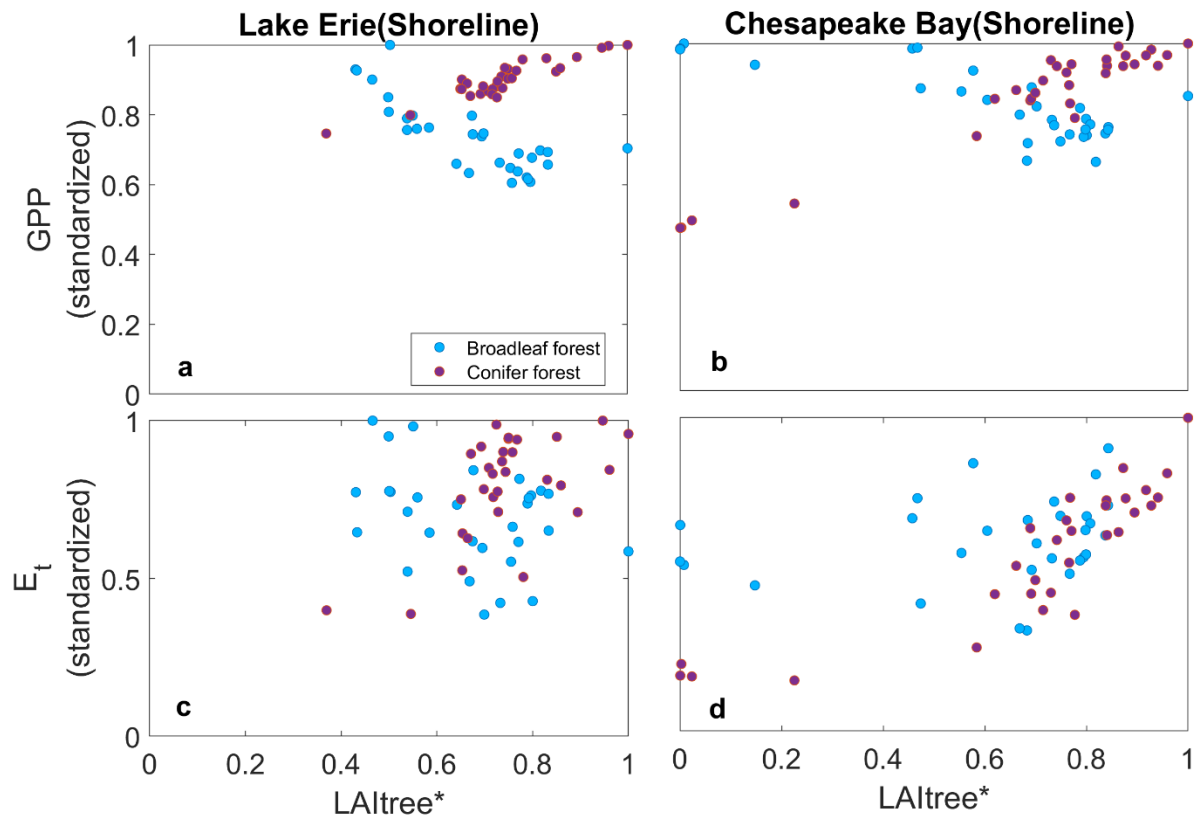


Fig.8

